Materials Advances

ROYAL SOCIETY OF CHEMISTRY

PAPER

View Article Online
View Journal

Cite this: DOI: 10.1039/d6ma00287k

Electrochemical carbon deposition from CO_2 in molten carbonates: substrate-dependent growth

Ivy Wu, [a] Samuel M. Pennell, [a] Haley Hoover, [a] Tolga H. Ulucan, [b] Drew J. Pereria, [a] Demelza Wright, [a] Oluwatamilore Olushina, [a] Nicholas A. Strange, [b] Kerry C. Rippy [a] and Robert T. Bell *[a]

Received 2nd March 2026,
Accepted 31st May 2026

DOI: 10.1039/d6ma00287k

rsc.li/materials-advances

Electrochemical carbon deposition from molten carbonate salts using inert electrodes and no additional catalyst is systematically examined. At sufficiently cathodic potentials, carbon formation occurs within 30 min and transitions from substrate-dependent nucleation to carbon-on-carbon growth. Although deposits formed on either mild-steel or graphite cathodes exhibit comparable thicknesses and salt contents, their macrostructures differ, reflecting differences in early-stage growth rates and surface chemistry. Characterization by ICP-OES, Raman spectroscopy, SEM/EDS, synchrotron powder X-ray diffraction, and C K-edge X-ray absorption near edge structure reveals that the as-deposited carbon is predominantly disordered sp^2-bonded material. However, post-treatment reveals latent turbostratic ordering in select samples, indicating that short-range order is established during deposition but is obscured by an entrained electrolyte and kinetically formed amorphous phases. No anode-derived contamination is detected, and carbon grown on graphite cathodes shows minimal metallic impurities. These results clarify the role of cathode surface chemistry and provide pathways for controlling electrode-derived impurity incorporation and carbon structure in catalyst-free molten carbonate systems.

Introduction

Solid carbon plays a critical role across modern industries, serving as a key material in fuel production, metallurgy, and energy storage. Specific carbon allotropes such as graphite and graphene are of particular technological importance due to their electrical and thermal conductivity combined with high chemical and thermal stability. In particular, graphite remains the dominant anode material in lithium-ion batteries—a market projected to expand fivefold by 2050[1]—and is also a key electrode material in primary metal production, including steel and aluminium manufacturing. Owing to its strategic importance and limited reliable supply, graphite has been designated a critical mineral by both the United States and the European Union.

Graphene, the 2D version of graphite, is used in electronics, sensors, and in composite materials, with global production at 23 000 metric tons.[2] More recently, turbostratic graphene—characterized by rotationally misaligned graphene layers—has attracted significant interest due to its unique electronic properties, including twist angle-dependent superconductivity, and its relevance in spin devices, magnetic memories, and energy storage systems.[3,4] Demand is further intensified by the acceleration of commercial developments leveraging graphene in new applications such as concrete and asphalt. Similarly, the demand for amorphous carbon such as carbon black in tires is a US$28 billion industry that continues to grow.[5]

Despite the high value and growing demand for carbon across different industries, inexpensive and scalable methods of producing carbon and structured carbon remain limited. Natural graphite deposits are geographically constrained and often compositionally heterogeneous, necessitating mixing with synthetic graphite to meet performance requirements.[6] Conventional synthetic graphite production methods are costly, relying on temperatures reaching 3000 °C and days of processing. These costs of synthetic graphite production are an order of magnitude higher than those of natural graphite mining (7000–20 000 $ per t *vs.* 600–2070 $ per t).[1] There is sustained interest in alternative graphite and carbon production pathways, including pyrolyzed biomass,[7] thermochemical reduction of CO/CO_2,[8] and molten salt electrochemical conversion of CO_2.[9–12]

Carbon can be produced *via* electrodeposition from molten salts, a process established at the bench scale in the 1960s[13,14] and has since been revisited. Zhu *et al.* reported the energy consumption of electrochemical graphite production to be in the range of 4.5–5.5 kWh per kg C, significantly lower than the traditional high-temperature process of 32.1 kWh per kg C.[15]

[a] *National Laboratory of the Rockies, Formerly National Renewable Energy Laboratory, 15013 Denver West Parkway, Golden, CO 80401, USA. E-mail: robert.bell@nlr.gov*
[b] *SLAC National Accelerator Laboratory, 2575 Sand Hill Rd, Menlo Park, CA 94025, USA*

In these systems, carbonate ions are electrochemically reduced to solid carbon at the cathode (Reaction (1)), while the electrolyte is regenerated through reaction with CO_2 (Reaction (2)) at temperatures between 500 and 900 °C.

$$CO_3^{2-} + 4e^- \rightarrow C + 3O^{2-} \quad (R1)$$

$$CO_2 + O^{2-} \rightarrow CO_3^{2-} \quad (R2)$$

At an inert anode, the generation of O_2 and/or CO_2 can occur, as shown in Reactions (3) and (4).

$$2O^{2-} \rightarrow O_2 + 4e^- \quad (R3)$$

$$2CO_3^{2-} \rightarrow 2CO_2 + O_2 + 4e^- \quad (R4)$$

Overall, the reaction is the decomposition of CO_2:

$$CO_2 \rightarrow C + O_2 \quad (R5)$$

Recent studies have explored carbon formation from molten alkali carbonates (Li_2CO_3, Na_2CO_3, K_2CO_3, or mixtures) with metallic cathodes (Ni, Fe, Pt, or Cu) which can act as catalytic or nucleation surfaces for carbon deposition.[16–20] Transition metal cathodes, such as Ni, have been shown to catalyse this type of growth,[21] forming nanotubes and amorphous, platelet, spherical, or ordered morphologies depending on deposition conditions.[22–24] Tang *et al.* produced carbon powders on Ni cathodes and inert SnO_2 anodes at high voltages (3–6 V) and found co-deposition of alkali salts with varied carbon forms, including nanoparticles, nanoflakes, nanosheets and heart-shaped nanostructured cages, with particle sizes ranging from 50 nm to 2 μm depending on electrolysis time and temperature.[25] However, molten salt carbon deposition systems commonly require deposition times of 1 h or longer, operate at high polarization (3.5–5.0 V), and exhibit current densities in the range of 50–300 mA cm^{-2}, leading to an energy consumption of 35–54 kWh kg^{-1} and frequent incorporation of metallic impurities.[12,26]

Extended operation (>1 h) at high polarization exacerbates metal contamination, particularly from Ni, Cr, and Fe, which degrades carbon purity and complicates downstream use.[15–18,26–28] Although the use of inert anodes such as Pt or SnO_2 mitigates anode contamination,[12,29–31] cathode-derived impurities remain a persistent challenge. Therefore, we suggest that similarly replacing the cathode with a carbon material such as graphite to grow carbon-on-carbon could further reduce these impurities by eliminating Ni, Cr, and Fe from the electrochemical cell. Given that carbon prices scale strongly with purity—amorphous carbon containing 60–90% graphite is valued at an order of magnitude less than crystalline graphite[1] with a purity of 90–99.95% —there is an economic incentive to eliminate metal-derived contamination at its source. Direct growth of carbon on graphite therefore represents an avenue for producing higher-purity carbon materials.

Electrochemical formation of carbon from CO_2/carbonate in molten carbonate media has been demonstrated previously and applied toward functional carbon materials, including CO_2-derived nanoscale supports and carbon-based composites.[32,33] The present work goes beyond demonstration by examining how the cathode substrate governs early-stage deposit architecture and salt entrapment, and by showing that post-treatment can expose a more ordered carbon component, as detected by C K-edge XANES—an effect not apparent from macroscopic inspection of the as-deposited material. Despite sustained interest in molten carbonate systems, few studies systematically address how the carbon macrostructure changes during deposition or the influence of the underlying surface on the formed carbon structures. For example, Hughes *et al.* reported substrate-dependent differences in lattice spacing for graphitized carbon deposited on Au, Cu, and graphite electrodes but no further investigations or explanations were given.[34] Detailed characterization of the deposition process and resulting product is needed for a complete understanding of carbon formation in molten electrochemical systems.

In this work, we examine carbon deposition from CO_2 in molten Li–K carbonate salts using either mild steel or graphite cathodes and an inert SnO_2 anode, with emphasis on how cathode substrate chemistry governs early-stage growth behavior, macroscopic deposit architecture, and electrolyte entrapment. This study aims to resolve how substrate-dependent nucleation transitions to carbon-on-carbon growth under kinetically driven deposition conditions. Importantly, we show that post-deposition treatment enabled exposure of latent ordered sp^2 stacking that is not evident in as-deposited materials. This effect is resolved using C K-edge X-ray absorption near-edge structure spectroscopy, providing direct insight into heterogeneous carbon architectures generated during molten carbonate electrochemical reduction. Together, these results establish a mechanistic link between substrate chemistry, deposit morphology, and the spectroscopic emergence of locally ordered carbon domains in catalyst-free molten salt systems.

Results and discussion

Electro-reduction of carbonate to carbon

A schematic of the electrochemical reactor is shown in Fig. S1. Cyclic voltammetry on either graphite or steel cathodes was performed at 10 mV s^{-1} in a 2-electrode system with SnO_2 anodes and shown in Fig. S2. A reduction peak at −1.6 V is observed with the steel cathode but is absent on the graphite cathode, suggesting different reduction mechanisms or reduction reactions associated with transition metals present only in steel. Both systems show cathodic current limits at −2.0 V. High and low potentials of −1.8 V and −2.4 V were chosen for chronoamperometry on a steel cathode to assess the viability of carbon deposition under these different voltage conditions. No carbon was observed to agglomerate at the surface of the steel cathode after 28 min at −1.8 V while copious carbon was deposited at −2.4 V, supporting the explanation that transition metal reduction reactions not associated with carbon deposition occur below −2 V. Therefore, the chronoamperometry results from steel and graphite electrodes at −2.4 V, sufficient for carbon deposition, are shown in Fig. 1.

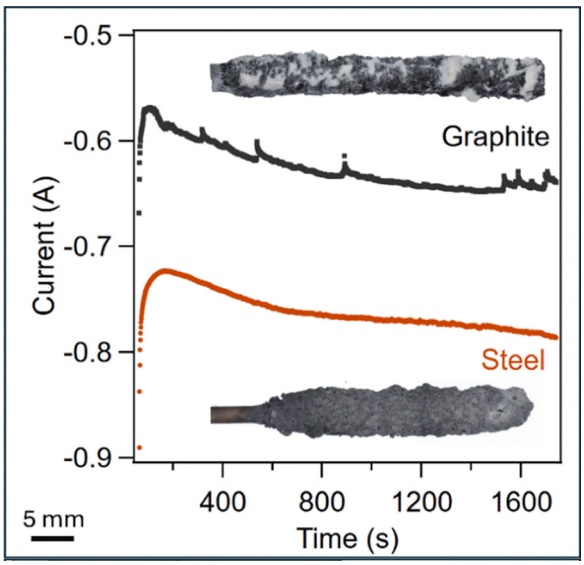

Fig. 1 Current response to 28 min of chronoamperometry using a steel cathode (orange), and a graphite cathode at −2.4 V (black).

The current response shows a steady increase under the −2.4 V condition for both graphite and steel electrodes. The higher current observed on steel is likely related to the ability of transition metals in steel to catalyze the deposition reaction. Notably, both steel and graphite electrodes exhibit a similar rise in current suggesting that after formation of an initial deposit layer of carbon on steel, the reaction proceeds by depositing carbon on carbon.

Rough, black deposits were observed on both samples, which completely encompass the electrodes while entraining salt within the deposit. The growth of these conductive carbons fully covering and growing on the electrodes effectively increases the electrode surface area over time. On observation of the cross-sectional optical images (Fig. 2a and b), salt-rich areas (red arrows) are seen entrapped in the dark carbon deposits (yellow arrows) on both steel and graphite electrodes. Digital image analysis was used to estimate the relative amounts of carbon : salt from the cross-sectional images. Since salt appears white and carbon appears black, thresholding can be used to differentiate them in the images. The areas exterior to the sample and the electrode were excluded, and then the image was binarized with a manually applied threshold. The relative areas of the carbon and salt were then calculated to be 57 : 43 carbon : salt for both electrodes. The thresholded images used for analysis are shown in Fig. S3.

Despite a similar overall thickness and salt content of the deposit on steel and graphite (~ 1 mm, 43%), the macroscopic structure of the deposits vary substantially. Near the graphite electrode surface, the carbon deposit shows little to no salt entrapment, with greater salt incorporation as the deposit grows beyond 200 μm and resulting in non-concentric growth around the cylindrical electrode. This behavior is consistent throughout the length of the electrode. In contrast, the steel electrode shows radially consistent salt entrapment throughout the deposit, with band-like formations of denser carbon that do not span the entire circumference but appear to striate along the length of the rod. This phenomenon could be due to the

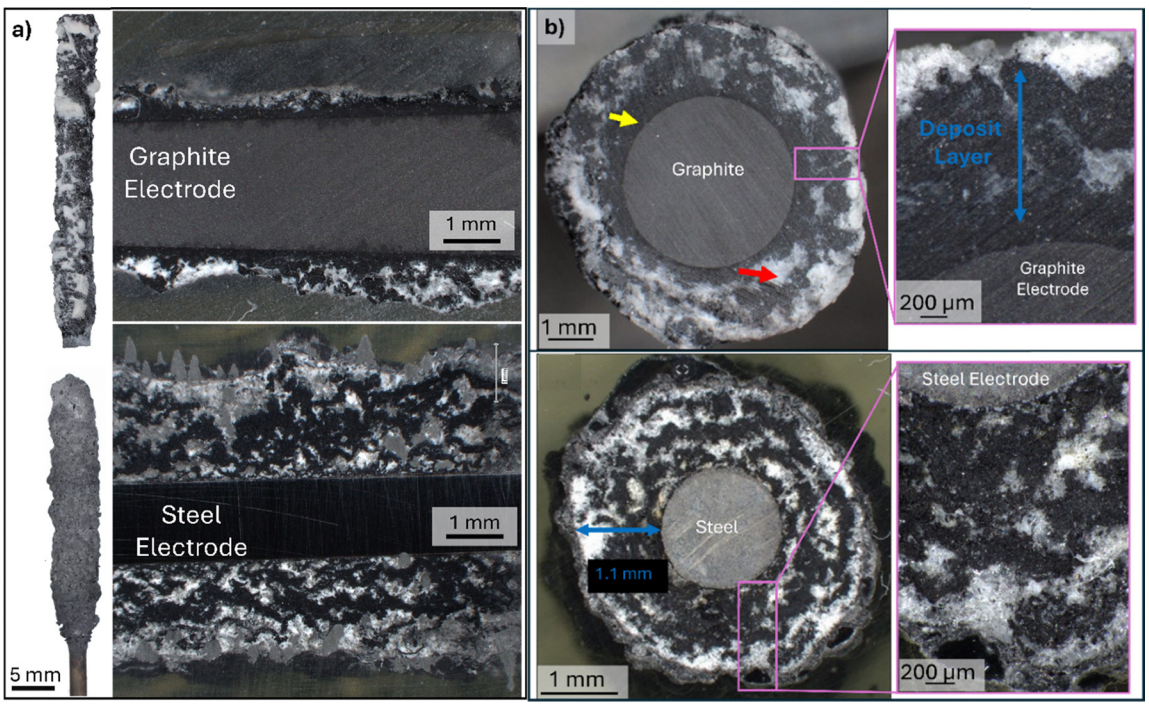

Fig. 2 (a) Longitudinal and (b) cross sectional optical micrographs after applying a cell potential of −2.4 V on graphite and steel cathodes. The red arrow marks the recrystallized salt.

different surface properties of the electrodes and the relative rates of the reaction.

Transition metals in steel initially catalyze the carbon deposition reaction, causing rapid carbon growth (a high current of ~0.72 A), which inadvertently entraps salt and increases the surface area by adding to the conductive electrode surface. Additionally, the mixture of metals in steel and the presence of surface oxides and passivation layers inherently lead to greater surface inhomogeneity, which could result in locally variable carbon growth and greater salt entrapment in the initial stages of deposition on steel compared to the smooth and homogeneous surface of the graphite electrode. Without these catalysts and inhomogeneities, carbon growth directly on graphite is slower, which results in less salt entrapment and initially concentric carbon growth. As the carbon encompasses the surface, the electrochemical reaction transitions from carbon-on-steel or carbon-on-graphite to carbon-on-carbon. At this stage, the deposition reaction becomes substrate-blind and the change in the growth rate of carbon is similar on both cathodes, with an ~200 mA shift in current due to the higher surface area of the nonhomogeneous carbon growth on steel. These results highlight the effect that the electrode surface properties have on the quantity and macrostructure of carbon deposited.

Characterization of carbon deposits

Acid washing of as-deposited carbon layers consistently triggered rapid gas evolution and mechanical destabilization of the deposits. In the case of samples grown on graphite cathodes, this behavior was accompanied by detachment of carbonaceous material from the underlying graphite substrate, likely arising from mechanical weakening during electrolyte removal. These observations indicate that the deposited carbon forms a weakly consolidated, salt-supported network generated under kinetically driven growth conditions. Accordingly, the results presented below focus primarily on the characterization of the as-deposited materials to preserve the native growth architecture and to elucidate the role of substrate chemistry and deposition kinetics in governing deposit structure.

Raman spectroscopy was conducted to investigate the structural evolution of the as-deposited carbon as a function of distance from the electrode surface (Fig. 3). The spectra were collected at multiple locations along the cross section of the carbon layer, with care taken to avoid salt-rich regions, to assess gradients in graphitic ordering within the deposit. For the steel substrate, the higher degree of salt entrapment, as discussed in Fig. 2, limited the ability to sample salt-free regions. As a result, large broadband fluorescence and elevated background emissions obscured the Raman features of the steel sample, shown in Fig. S4, at both 633 nm and 785 nm wavelengths. The presence of Fe within these salt deposits, indicated by the pink coloration of the salt after testing and confirmed by ICP analysis (Table S1), is likely responsible for these interfering effects. Fe can complex with carbonate ions to form oxides/hydroxides that exhibit strong fluorescence.[35] In particular, siderite ($FeCO_3$) displays a Raman-active ν_1 mode at 1085 cm^{-1}.[36] In contrast, the lower degree of salt entrapment and the absence of Fe in the carbon deposits formed on graphite enabled acquisition of high signal-to-noise spectra, showing the characteristic D (~1350 cm^{-1}) and G (~1582 cm^{-1}) bands.

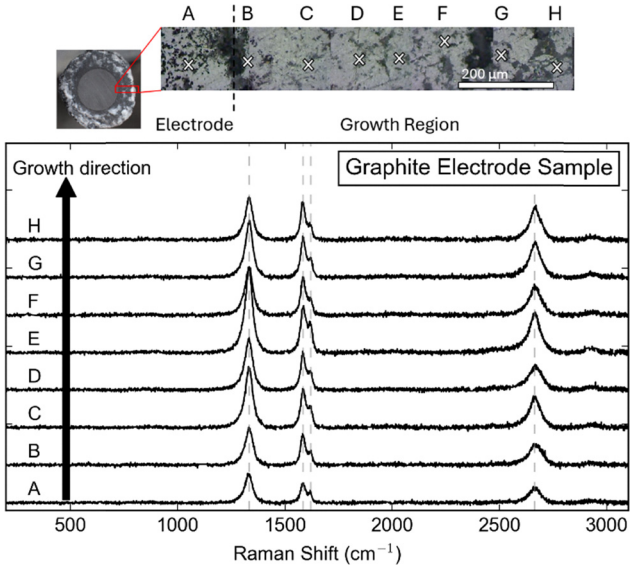

Fig. 3 Raman spectra collected at varying points on the carbon deposited on the (a) steel cathode and (b) graphite cathode. Point A is on the electrode.

Notably, the relative intensity ratio of D/G calculated using Renishaw WiRe™ 5.6 software based on peak heights using a mixed Gaussian–Lorentzian fit is 1.476 on the graphite rod, consistent with graphite electrodes, which have been exposed to high temperatures.[37,38] The relative peak height intensity ratio of *D*/*G* remains largely consistent ranging from ~1.0 to 1.6 across the sampled regions of the deposit, as listed in Table S2. All fits are displayed in Fig. S5. This trend suggests that the structural ordering and defect density of the carbon phase remain relatively uniform throughout the deposition layer, with no significant gradient in carbon quality as the film grows on graphite. These observations indicate that under the applied electrochemical conditions, carbon deposition on graphite proceeds *via* a steady growth mechanism that preserves the degree of local ordering in the sp^2 carbon network. The uniformity in Raman response further supports that once an initial carbon layer is established, subsequent deposition occurs on carbon itself, leading to consistent growth kinetics.

Scanning electron microscopy (SEM) with energy dispersive X-ray spectroscopy (EDS) was used to investigate the microstructure of carbon deposits. EDS was used to identify the grains belonging to carbon *vs.* entrained salt (Fig. S6). Fig. 4a–c shows electron micrographs of the denser carbon region near the buried graphite electrode surface, and Fig. 4d shows various carbon phases deposited on steel.

Two distinct phases with different brightness were observed, which are attributed to the carbon-rich phases of different morphologies (yellow arrows, Fig. 4a and b) and K- and O-rich phases (red arrow, Fig. 4a). These K- and O-rich phases are assumed to be recrystallized salt or related compounds (oxides

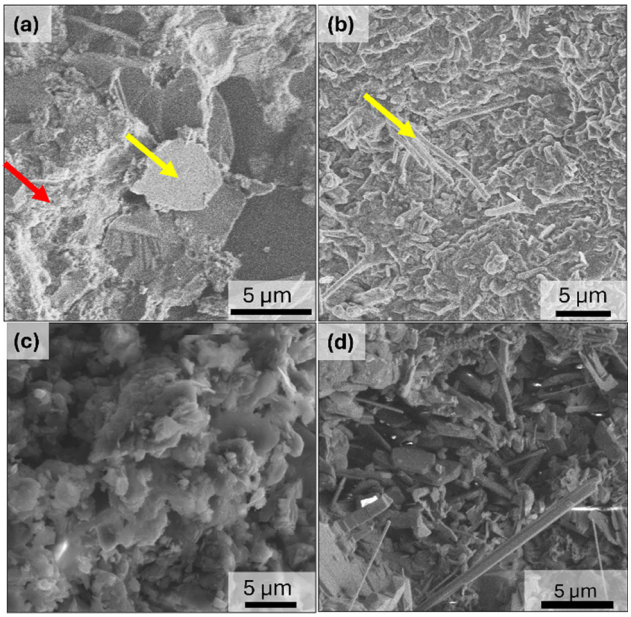

Fig. 4 Electron micrographs of the carbon deposit layer on graphite electrodes at −2.4 V showing (a) flakes, (b) rod-like structures, and (c) amorphous phases interspersed with salt. (d) Structures of the carbon deposited on steel. Yellow arrows mark carbon phases; red arrows mark recrystallized salts.

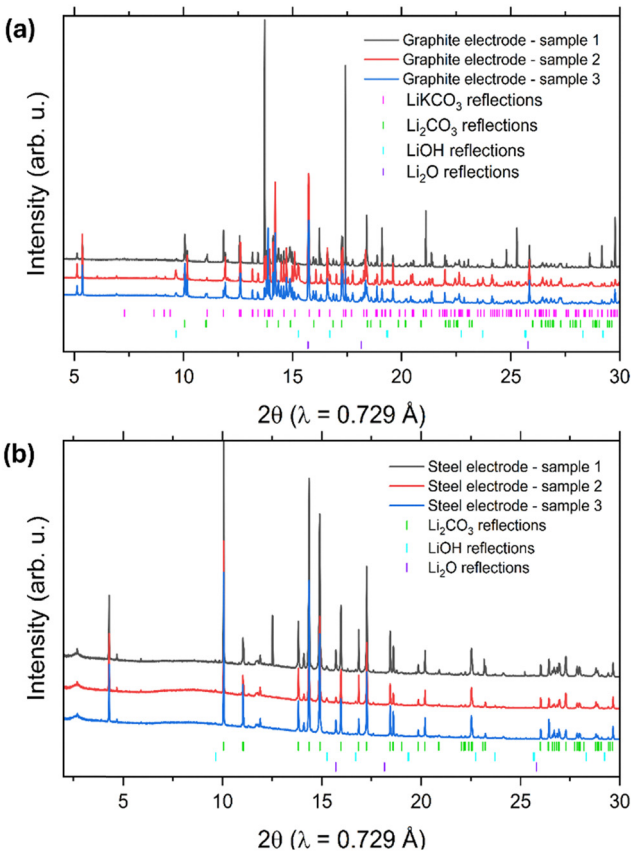

Fig. 5 PXRD patterns of (a) graphite electrode precipitates and (b) steel electrode precipitates. All three diffraction patterns of the three sample aliquots are shown with reflections associated with identified structural phases.

and hydroxides), which become trapped in the growing carbon layer. The ∼5 μm carbon flakes shown in Fig. 4a are indicative of graphitic carbon. Additionally, rod-like (Fig. 4b) and amorphous (Fig. 4c) carbon structures were observed on the same deposit layer, indicating the variety of carbon structures that are produced. The diversity of structures implies that there are different mechanistic parameters that affect the resulting architecture, which is not solely dependent on the distance from the graphite rod during deposition. The carbon phases on steel (Fig. 4d) similarly show a mixture of rods/whiskers and flakes distributed throughout the deposit.

To further probe the phases and local atomic structure of the deposited carbon layers, the deposit was removed and crushed for investigation using synchrotron radiation techniques. Fig. 5a and b show the XRD patterns of deposits formed on graphite and steel cathodes after removal and grinding *via* a mortar and pestle.

Three capillaries of each electrode/preparation process were measured using synchrotron PXRD. These samples displayed visual heterogeneities, which were also apparent in the PXRD data. The graphite electrode sample demonstrated the greatest quantity of distinguishable structural phases, which included the $LiKCO_3$ precursor salt, Li_2CO_3, LiOH, and Li_2O, as shown in Fig. 5a. The remaining structures could not be identified from related compounds (*e.g.*, K_2CO_3, mixed Li–K oxides, or mixed Li–K hydroxides) or indexing methods, presumably due to the number of unidentified structures. Interestingly, K-containing compounds were unidentified, with exception to the mixed $(Li,K)_2CO_3$. It is possible that the low angle (2θ = 4–5.5°; d ∼ 7.6–10.4 Å) reflections are associated with the interlayer spacing of disordered Li- and/or K-intercalated graphite structures but could not be absolutely verified. There are reflections in all three samples present at ∼12.6° (d = 3.32 Å), potentially related to the 002 reflection of graphite, which is often observed with d = 3.34 Å. However, additional reflections associated with graphite were not observed, which indicate that any graphite is turbostratic and exhibits disordered in-plane.

Diffraction from the unrinsed steel electrode (Fig. 5b) largely demonstrated characteristics similar to the graphite electrode with one key exception – the $LiKCO_3$ reactant was not observed. Also, the low angle reflections are present with dissimilar d-spacings. The graphite 002 reflection was less apparent in the steel electrode, save for an intense reflection at 2θ = 12.523°, associated with an intense Bragg spot in the 2D data. Interestingly, when this sample was re-measured four months later, the data waere easily represented by 92 wt% Li_2CO_3 and 8 wt% graphite (see Fig. S7 and Tables S3–S5 for refinement parameters). We note that heterogeneity in the samples limits the precision of these quantitative values; however, these results qualitatively demonstrate the presence of graphitic carbon in the sample. It is not clear if the change in the observed data comes from the reaction of residual oxides/hydroxides from ground powder with atmospheric CO_2 *via* an enhanced surface area or is purely a result of sample heterogeneity.

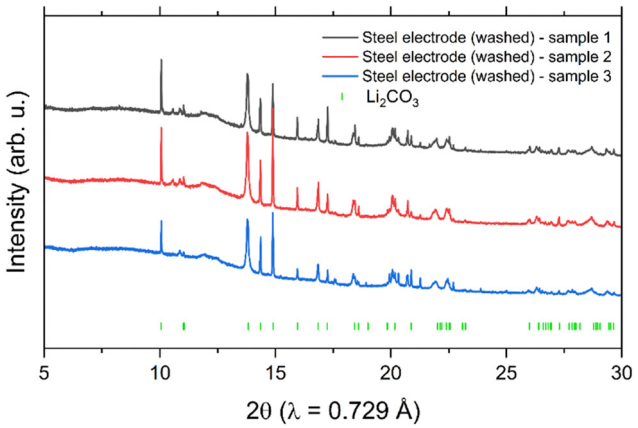

Fig. 6 PXRD patterns of deposits formed on the steel electrode after acid washing.

When the steel electrode is washed with acid, the observed diffraction changes yet again, as illustrated in Fig. 6. Here, the PXRD data are represented by Li_2CO_3 with subtle contributions from secondary phase(s) and a more prominent background, likely from a greater amorphous fraction. In the PXRD patterns of these samples, there are no low angle/large *d*-spacing reflections. In contrast, acid washing of as-deposited carbon layers on graphite cathodes induced rapid gas evolution and severe mechanical disruption of the deposits, including detachment of the carbonaceous material from the underlying graphite rod. This disruption and contamination alter the sample and therefore conclusions could not be accurately determined from the washed graphite samples.

To further investigate the ordered nature of the carbon deposit, X-ray absorption near edge structure (XANES) was employed to characterize the carbon deposited on both steel and graphite substrates, as well as in a washed variant of the steel-supported sample. These results are shown in Fig. 7.

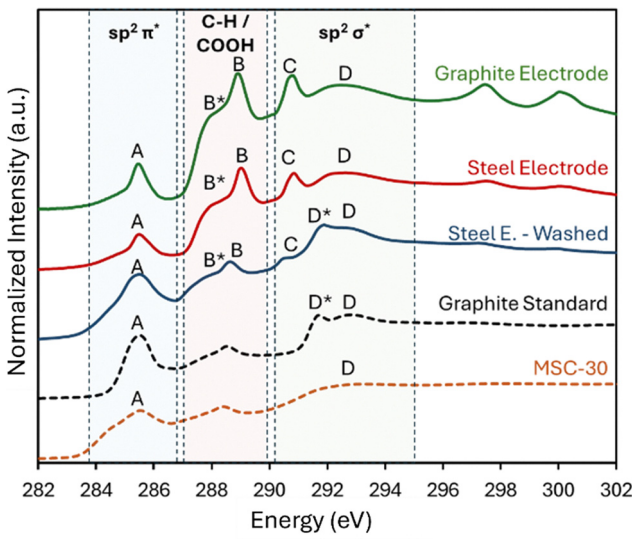

Fig. 7 Total electron yield (TEY) C 1s spectra of the (green), (red) and (blue) samples. Dashed lines belong to graphite (black) and MSC-30 (orange) standards. Three characteristic regions of the spectra are highlighted, and the respective peaks are labelled to guide the reader.

C K-edge XANES probes the electronic structure and bonding environments in the carbon deposit, providing insight into both the local bonding geometry and long-range ordering of the carbon network as influenced by the deposition substrate and subsequent washing.

All samples exhibit a π* resonance centered at ~285.5 eV, indicative of sp^2-hybridized carbon.[39–42] The sharpness and consistent energy position of this peak across the steel electrode, graphite electrode, and washed samples suggest that the local bonding environment is dominated by planar C=C motifs, largely independent of the substrate or processing. The alignment of these features with the π* resonance of graphitic standards confirms reliable energy calibration and supports the conclusion that π* states are robust against structural disorder at the scale of nearest-neighbor interactions.[43,44] Compared to the MSC-30 standard, samples have relatively sharper π* resonance, affirming the higher degree of structural order.

The presence and clarity of the π* peak—together with the absence of spectral signatures associated with sp^3-hybridized carbon—suggests that the electrochemical deposition process does not result in amorphous carbon formation. However, the absence of a well-defined long-range order sp^2 excitonic peak (D*) at ~291.7 eV in the steel and graphite electrode samples, alongside the emergence of a broad, redshifted σ*-like feature (C) centered at ~290.7 eV, indicates that these materials lack the interlayer coherence characteristic of crystalline graphite. These specific spectral signatures were measured by total-electron-yield C K-edge XANES. The suppression of the D* excitonic resonance, despite the persistence of a sharp π* feature and concomitant broadening of the σ* region, constitutes a diagnostic XANES fingerprint of turbostratic graphitic domains—sp^2-rich carbon regions that preserve in-plane ordering while exhibiting rotational or translational disorder between adjacent layers.[45–47] This structural motif reflects a partially ordered form of graphitic carbon that retains π-conjugation locally while lacking long-range stacking order.

In the functionalized carbon region (C–H/COOH) between the π* and σ* resonances, all samples exhibit two characteristic features: a broad shoulder near ~288 eV and a sharper peak at ~289 eV. These features are frequently reported in the carbon K-edge spectra of disordered graphitic materials and are often associated with structural disorder or oxygen-containing functionalities. The exact identification of these features requires complementary spectroscopic techniques, but these features were frequently assigned to C–H and COOH groups in the literature.[48–53]

In the graphite standard, a sharp long-range order sp^2 excitonic peak (D*) at ~291.7 eV confirms the expected crystallinity.[5,6,15,16] In contrast, the steel and graphite electrode samples display a broadened and redshifted feature (C), consistent with σ*-like transitions into localized states that likely arise from turbostratic stacking, constrained domain sizes, and bond angle disorder. Instead, these samples only form broad σ* sp^2 peaks (D). These effects suppress the formation of an

excitonic resonance, reflecting a disordered carbon architecture with limited coherence lengths.

Post-treatment produces the most structurally informative change observed in this study. While the as-deposited carbons are dominated by disordered sp^2 bonding and substantial electrolyte-associated contributions, acid washing of the steel-supported deposits to remove surface-bound impurities and disordered phases shows a notable spectral transformation. The broad, red-shifted σ*-like feature (C) at ~290.7 eV diminishes significantly in intensity, while a weak but distinct shoulder (D*) appears at ~291.7 eV—precisely the energy of the long-range order sp^2 peak in graphitic carbon.[5,6,16] This emergence implies that the washing process either exposes previously buried ordered regions or facilitates a local reorganization of carbon layers. Rather than amorphizing the material, the post-treatment appears to selectively attenuate the contribution of highly disordered components, enhancing the spectral visibility of residual ordered domains.

These observations from the XANES data delineate a clear structural progression: between crystalline graphite (standard) and short-range ordered MSC-30, the samples exhibit partially ordered yet intact sp^2 bonding (steel and graphite electrode samples), to a partially restored or exposed long-range ordering after washing. The final spectral observations are the residual potassium L-edge features at ~297.5 and ~300.2 eV that correspond to $2p_{3/2}$ and $2p_{1/2}$ transitions.[54–56] These residual K^+ ions from $LiKCO_3$ appear to be higher in the graphite electrode compared to steel and decrease with the washing process.

The presence of electrode-derived impurities in the deposited carbons was evaluated by inductively coupled plasma optical emission spectrometry (ICP-OES). It should be noted that optical microscopy and diffraction highlight localized regions of electrolyte entrapment within the deposits, whereas the ICP–OES results reflect the bulk composition of the selectively sampled, carbon-rich fraction analyzed after digestion. For each sample, a representative portion of the deposit was selected for digestion, with deliberate avoidance of salt-rich regions. No Sn was detected in any of the samples, suggesting that the SnO_2 anode is a robust choice as an inert counter electrode. Li, K, and Fe were detected on the steel sample consistent with uniform electrolyte entrapment within the deposit and incorporation of steel-derived species during growth. In contrast, no metallic impurities were detected on the sample grown on graphite. The absence of Li and K in this case reflects the heterogeneous distribution of the entrained electrolyte within the deposit and the localized, carbon-rich regions selected for analysis. These results demonstrate the potential utility of this system. The full list of tested elements and testing parameters is provided in Table S1.

Overall, we have demonstrated electrochemical deposition of turbostratic sp^2 carbon on mild steel or graphite cathodes and SnO_2 anodes with no additional catalyst. While not fully graphitic, turbostratic carbons possess local ordering and can serve as an indicator of initial graphitization, indicating the utility of this structure in the production of other useful carbon phases such as needle coke. Our process shows tunability from amorphous to ordered carbons.

Conclusions

Rapid electrochemical deposition of carbon from molten carbonate salts onto either mild steel or graphite electrodes with inert SnO_2 anodes and no additional catalyst was demonstrated. Acid washing the carbon deposit revealed turbostratic sp^2 carbon deposited on steel, perhaps indicative of the changing nature of the deposit during deposition. With no detectable Sn observed to contaminate the carbon deposit on either electrode, our system is robust and further tuning of the applied potential, time, and temperature will influence the carbon deposition route and resulting morphology.

- On both graphite and steel electrodes, the rapid <30 min deposition of carbon is observed, with both amorphous and ordered carbon phases observed.
- For mild steel electrodes, the deposition of carbon on the surface immediately entrapped salt, which was encased within the growing carbon layer.
- For graphite electrodes, the growth of the deposit layer was slower than that of the steel electrode and initially formed a salt-free carbon rich layer, with greater salt entrapment as the layer grows.
- Tuning the carbon deposition rate through applied voltage and surface properties appear to be viable pathways to reduce salt entrapment.

These carbon deposition reactions in our system show promise for the production of metal-free ordered solid carbon products including graphite. Understanding their growth during electrodeposition is key towards development of a tightly controlled process optimized for greater graphitic structures, with less entrapped salt.

Experimental

Materials

Lithium carbonate (≥99%, Sigma Aldrich) and potassium carbonate (≥99%, Sigma Aldrich) were used as received. Mild steel rods (AISI 1018, diameter: 2 mm; length: 300 mm, McMaster-Carr), SnO_2 rods (purity: 98.5%; diameter: 10 mm; length: 300 mm, Dyson Industries Ltd.), and conductive graphite rods (diameter: 3.175 mm; length: 300 mm, McMaster-Carr) were used as electrodes. Alumina sheaths and crucibles were purchased from AdValue Technology (AL-T-N1/4-N3/16-12).

Salt preparation

A mixture of Li–K carbonates was adopted for this study. Salts were stored and prepared in a N_2 glovebox by bulk mixing the lithium and potassium carbonate in a 1 : 1 molar ratio and adding ~200 g of this mixture to a pre-weighed alumina crucible. Shortly before testing, the filled crucibles were removed from the glovebox and quickly inserted into a furnace.

Reactor setup

A high Ni-steel bucket and lid were used in a Thermo-Fisher Scientific CF56622C Lindberg/Blue M™ Crucible Furnace. The reactor was assembled with electrodes pre-immersed in the

solid powdered electrolyte, shielded from electrical contact with the bucket lid *via* alumina sheaths, and electrically connected with Cu wire for contact with potentiostat leads. A type-K thermocouple enclosed in a closed end alumina tube was held at the center of the crucible, in the electrolyte. A multiple-bore hole alumina tube was also immersed into the electrolyte to pump gas. The bucket was sealed with Swagelok fittings and PTFE ferrules. A schematic of the reactor is shown in Fig. S1.

The Cu wires connecting the electrodes were attached in a 2-electrode configuration to an Autolab Vionic Potentiostat/Galvanostat 3500001080) for electrochemical measurements and data were collected using Intello software. The measured voltages were internally referenced against the oxygen evolution reaction occurring at the anode, which is assumed to be relatively stable in the short time spans of the electrochemical experiments.

Electrochemical testing

Argon gas was pumped into the apparatus for ~12 h at a flow rate of 90 sccm to purge the reactor prior to testing. To conduct testing, the furnace was first heated to 200 °C at a rate of 5.8 °C min^{-1} and held for 1 h to remove the remaining moisture. At this stage, pure CO_2 was introduced into the cell at 150 sccm, and the furnace was then ramped to 800 °C at a rate of 4 °C min^{-1} and held for 1 h prior to electrochemical testing.

All chronoamperometry and cyclic voltammetry tests were carried out in a two-electrode configuration in the same electrolyte (50/50 mol% Li_2CO_3 : K_2CO_3), bath temperature (715 °C), and anode (SnO_2). Cyclic voltammetry tests were swept in the cathodic direction at 20 mV s^{-1} and chronopotentiometry tests were held at either −1.8 or −2.4 V for 28 min. Immediately after electrochemical testing, the electrodes were lifted above the molten electrolyte and allowed to dangle in the headspace while continuing to flow CO_2 through the reactor. The system was allowed to naturally cool to ambient temperature, ~4 °C min^{-1}.

Characterization

After cooling, the electrodes and attached deposit layer were imaged with a Keyence VHX 7000 optical microscope. The samples were sectioned into 1 cm segments with a diamond wafering blade, then mounted in epoxy (Buehler Epothin 2) for mechanical cross-sectioning. After the epoxy cured, the samples were ground to P4000 grit with SiC grit sheets, then polished to 1 micron with diamond slurry. Electron microscopy characterization was performed on a ThermoFisher Nova 650, utilizing both SE and BSE detectors.

Raman spectra were acquired using a Renishaw inVia Raman Microscope with a 633 nm or 785 nm laser source (Coherent). Each spectrum was generated with a single accumulation in a range of 200–3100 cm^{-1}, using an exposure time of 20 s and a laser power of 0.6 mW over an excitation area of approximately 4 μm^2. Spectra were taken starting near the surface of the graphite or steel electrode, then moved outward in the growth direction of the sample while avoiding salt-rich areas. The various points of measurement are indicated in each figure. No normalization of signal intensity was performed on these data, but the data were formatted in a cascade-style plot for clarity. All raw spectra were cleaned of their cosmic rays using a customized python code that cleans data based on a threshold degree of peak intensity and interpolates regions where the spectra were removed (*i.e.*, cosmic rays tend to be very narrow and sharp compared to real signals). One additional broad cosmic ray was removed from the graphite electrode sample spectra from Location B, around 1100–1140 cm^{-1}. Key peaks for graphite are marked with a vertical dashed line in each figure. Renishaw inVia Raman Microscope WiRe™ 5.6 software was used to fit the spectra with a mixed Gaussian–Lorentzian fit and I_d/I_g ratios calculated from the peak heights.

Powder samples for Synchrotron measurements were prepared by gently mechanically removing the deposit from the electrode. For the washed steel samples, deposits were washed with 1 M sulfuric acid to remove the bulk of the entrained carbonate salts, then rinsed with DI water, collected on 11 μm Whatman filter paper, and dried for 8 h in a 60 °C oven. Powder X-ray diffraction (PXRD) measurements were performed at the Stanford Synchrotron Radiation Lightsource (SSRL) beamline 2-1. All samples were gently ground in an agate mortar and pestle and packed in ~0.7 mm o.d. Kapton capillaries. Given the visual heterogeneity, samples were prepared and measured in triplicate. Measurements were obtained using the robot-automated capillary powder diffraction capability described elsewhere.[57] Angle-dispersive 2D diffraction data were acquired stepwise between 2 and 113.55° two theta (q ~ 0.3–14.4 $Å^{-1}$). 2D images were normalized by incident beam intensity, stitched, and integrated using a python script developed specifically for use at beamline 2-1. CrystalDiffract was used to identify thestructural phases and Rietveld refinements performed using Topas Academic, version 7.[58]

Carbon K-edge X-ray absorption spectra were collected at beamline 8-2 of the Stanford Synchrotron Radiation Lightsource in total electron yield (TEY) mode under ultrahigh-vacuum conditions (10^{-8} Torr). The incident beam was focused to an area smaller than 1 mm^2, and a spherical grating monochromator was operated at an intermediate energy resolution of approximately 0.2 eV. Each sample was probed at three distinct locations on the surface, with two consecutive scans collected per location. The six individual spectra were averaged to obtain representative data while minimizing the influence of local heterogeneity. As a standard for comparison, Maxsorb® MSC-30 activated carbon (Kansai Coke & Chemicals Co., Ltd, Japan) was used. The energy scale was calibrated to the π* resonance of a synthetic graphite reference powder (Sigma-Aldrich, <20 μm, cat. no. 282863) at 285.5 eV, and the characteristic energy dependence of the incident light in the carbon absorption region was used to correct for possible beam energy drifts. Samples were mounted on an aluminium sample holder using double-sided copper tape and transferred into the measurement chamber. Data processing, normalization, and analysis were performed using the Athena and Fastosh software packages.[59,60]

Inductively coupled plasma-optical emission spectroscopy (ICP-OES) was performed on the deposit formed on either

graphite or steel cathodes. 1–10 mg samples of the deposit was mineralized in a Teflon tube with 9 mL of concentrated nitric acid and 3 mL of concentrated hydrochloric using a microwave digestion system (UltraWAVE 2, Milestone) at 1500 W following the UW-GE-4 method provided by Milestone. These samples were then diluted to 50 mL with MilliQ water and analyzed using an ICP-OES 5100 (Agilent Technologies Inc.). The method conditions and element wavelengths are listed in Table S1.

Faradaic efficiencies were calculated by washing the carbon deposits in acid and rinsing with DI water 3×, filtering through an 11 μm Whatman filter. This procedure induced rapid gas evolution from salt dissolution, readily breaking the salt-supported carbon into very fine fragments that are difficult to recover during filtration. The measured faradaic efficiency should therefore be regarded as a conservative lower bound.

The collected carbon on steel resulted in a 75% faradaic efficiency (FE) using the formula:

$$\mathrm{FE} = \left(\frac{nFm}{Q}\right)$$

where n = 4 moles of electrons, F = Faraday's number, m = moles of carbon collected, and Q = charge passed.

In the case of graphite cathodes, washing additionally caused detachment of the material from the underlying graphite substrate, introducing substrate-derived contamination. Consequently, the faradaic efficiency was quantified only for deposits formed on steel cathodes.

Author contributions

I. W and H. H: electrochemical investigation, methodology, visualization, validation, formal analysis, and writing – original draft; S. M. P: optical and microscopic investigations, methodology, visualization, validation, formal analysis, and writing; DJP and DW: Raman investigation and formal analysis; T. H. U and N. A. S: synchrotron data methodology, investigation, formal analysis, validation, visualization, and writing; O. O: investigation; K. C. R and R. T. B: writing – review and editing conceptualization, funding acquisition, and supervision.

Conflicts of interest

There are no conflicts to declare.

Data availability

Data are available upon reasonable request.

Supplementary information (SI): reactor schematic, CV, ICP data, additional Raman data, EDS map, and Rietveld refinement. See DOI: https://doi.org/10.1039/d6ma00287k.

Acknowledgements

The authors would like to thank Christopher Crain for assistance with PXRD measurements and Dennis Nordlund for XAS measurements. This work was authored by the National Laboratory of the Rockies (NLR), formerly National Renewable Energy Laboratory (NREL), for the U.S. Department of Energy (DOE) under Contract No. DE-AC36-08GO28308. This work was also supported by the Laboratory Directed Research and Development (LDRD) Program at the National Laboratory of the Rockies. Use of the Stanford Synchrotron Radiation Lightsource, SLAC National Accelerator Laboratory, was supported by the U.S. Department of Energy, Office of Science, Office of Basic Energy Sciences under Contract No. DE-AC02-76SF00515. The views expressed in the article do not necessarily represent the views of the DOE or the U.S. Government. The publisher, by accepting the article for publication, acknowledges that the U.S. Government retains a nonexclusive, paid-up, irrevocable, worldwide license to publish or reproduce the published form of this work, or allow others to do so, for U.S. Government purposes.

References

1 J. Zhang, C. Liang and J. B. Dunn, Graphite Flows in the U.S.: Insights into a Key Ingredient of Energy Transition, *Environ. Sci. Technol.*, 2023, **57**, 3402–3414.
2 T. Barkan, C. R. Ratwani, D. Johnson, K. Thodkar and C. Hill, Mapping the landscape for graphene commercialization, *Nat. Rev. Phys.*, 2024, **6**, 646–647.
3 K. V. Kumar, *et al.*, Exfoliation of graphite to turbostratic graphene, *2D Mater.*, 2024, **11**, 015022.
4 P. Kokmat, P. Surinlert and A. Ruammaitree, Growth of High-Purity and High-Quality Turbostratic Graphene with Different Interlayer Spacings, *ACS Omega*, 2023, **8**, 4010–4018.
5 Carbon Black Market Size, Share & Industry Analysis, By Process (Furnace Black, Thermal Black, Acetylene Black, and Others), By Grade (Standard Grade and Specialty Grade), By Application (Tire, Non-Tire Rubber, Inks & Toners, Plastics, and Others), and Regional Forecast, 2025-2032. 280 Source: https://www.fortunebusinessinsights.com/industry-reports/carbon-black-market-101718 (2025).
6 F. I. Barre, R. G. Billy, F. A. Lopez and D. B. Müller, Limits to graphite supply in a transition to a post-fossil society, *Resour., Conserv. Recycl.*, 2024, **208**, 107709.
7 Z. Sun, *et al.*, Preparation and formation mechanism of biomass-based graphite carbon catalyzed by iron nitrate under a low-temperature condition, *J. Environ. Manage.*, 2022, **318**, 115555.
8 C. Liang, *et al.*, Green synthesis of graphite from CO2 without graphitization process of amorphous carbon, *Nat. Commun.*, 2021, **12**, 119.
9 D. Bauer, R. Nguyen and B. Smith, *Critical Materials Assessment*, 2023.
10 Study on the Critical Raw Materials for the EU 2023 – Final Report.
11 S. Nasir, M. Hussein, Z. Zainal and N. Yusof, Carbon-Based Nanomaterials/Allotropes: A Glimpse of Their Synthesis, Properties and Some Applications, *Materials*, 2018, **11**, 295.

12 H. V. Ijije, R. C. Lawrence and G. Z. Chen, Carbon electrodeposition in molten salts: electrode reactions and applications, *RSC Adv.*, 2014, **4**, 35808–35817.
13 M. D. Ingram and G. J. Janz, The electrolytic deposition of carbon from fused carbonates, *Electrochim. Acta*, 1966, **11**, 1629–1639.
14 Y. U. K. Delimarskii, O. V. Gorodis'kii and V. F. Grishchenko, Cathode liberation of carbon from molten carbonate, *Dokl. Akad. Nauk SSSR*, 1964, **156**, 650–651.
15 F. Zhu, *et al.*, Molten salt electro-preparation of graphitic carbons, *Exploration*, 2023, **3**, 20210186.
16 B. Deng, *et al.*, Molten salt CO2 capture and electrotransformation (MSCC-ET) into capacitive carbon at medium temperature: Effect of the electrolyte composition, *Faraday Discuss.*, 2016, **190**, 241–258.
17 X. Wang, *et al.*, Magnetic carbon nanotubes: Carbide nucleated electrochemical growth of ferromagnetic CNTs from CO_2, *J. CO_2 Util.*, 2020, **40**, 101218.
18 X. Chen, *et al.*, Tuning the preferentially electrochemical growth of carbon at the ''gaseous CO2-liquid molten salt-solid electrode'' three-phase interline, *Electrochim. Acta*, 2019, **324**, 134852.
19 G. Chen, D. Min and Y. Huang, Electrochemical Mechanism of the Carbon Synthesis via Carbonate Ion Electroreduction in Molten Li_2CO_3–K_2CO_3 Mixture, *Electrochemistry*, 2022, **90**, 107004.
20 L. Hu, *et al.*, Direct Conversion of Greenhouse Gas CO_2 into Graphene via Molten Salts Electrolysis, *ChemSusChem*, 2016, **9**, 588–594.
21 R. Yu, *et al.*, Modulating carbon growth kinetics enables electrosynthesis of graphite derived from CO2 via a liquid–solid–solid process, *Carbon*, 2021, **184**, 426–436.
22 E. Laasonen, V. Ruuskanen, M. Niemelä, T. Koiranen and J. Ahola, Insights into carbon production by CO_2 reduction in molten salt electrolysis in coaxial-type reactor, *J. Environ. Chem. Eng.*, 2022, **10**, 106933.
23 W. Weng, B. Jiang, Z. Wang and W. Xiao, In situ electrochemical conversion of CO_2 in molten salts to advanced energy materials with reduced carbon emissions, *Sci. Adv.*, 2020, **6**, eaay9278.
24 Y. Cheng, *et al.*, The Effect of Molten Salt Composition on Carbon Structure: Preparation of High Value-Added Nano-Carbon Materials by Electrolysis of Carbon Dioxide, *Nanomaterials*, 2024, **15**, 53.
25 D. Tang, H. Yin, X. Mao, W. Xiao and D. H. Wang, Effects of applied voltage and temperature on the electrochemical production of carbon powders from CO2 in molten salt with an inert anode, *Electrochim. Acta*, 2013, **114**, 567–573.
26 A. Nur'aini, *et al.*, Comparative analysis of molten salt electrolytes for solid carbon production, *Renewable Sustainable Energy Rev.*, 2025, **209**, 115104.
27 G. Z. Chen, Interactions of molten salts with cathode products in the FFC Cambridge Process, *Int. J. Miner., Metall. Mater.*, 2020, **27**, 1572–1587.
28 E. Laasonen, *et al.*, The effect of metal dissolution on carbon production by high-temperature molten salt electrolysis, *J. CO_2* Util., 2023, **69**, 102390.
29 H. Yin, *et al.*, Capture and electrochemical conversion of CO2 to value-added carbon and oxygen by molten salt electrolysis, *Energy Environ. Sci.*, 2013, **6**, 1538.
30 H. V. Ijije and G. Z. Chen, Electrochemical manufacturing of nanocarbons from carbon dioxide in molten alkali metal carbonate salts: roles of alkali metal cations, *Adv. Manuf.*, 2016, **4**, 23–32.
31 H. V. Ijije, *et al.*, Electro-deposition and re-oxidation of carbon in carbonate-containing molten salts, *Faraday Discuss.*, 2014, **172**, 105–116.
32 G. Lacarbonara, S. Chini, S. Ratso, I. Kruusenberg and C. Arbizzani, A MnO_x–graphitic carbon composite from CO_2 for sustainable Li-ion battery anodes, *Mater. Adv.*, 2022, **3**, 7087–7097.
33 E. Najafli, *et al.*, Sustainable CO_2 -Derived Nanoscale Carbon Support to a Platinum Catalyst for Oxygen Reduction Reaction, *ACS Appl. Nano Mater.*, 2023, **6**, 5772–5780.
34 M. A. Hughes, R. D. Bennett, J. A. Allen and S. W. Donne, Physical characteristics of capacitive carbons derived from the electrolytic reduction of alkali metal carbonate molten salts, *RSC Adv.*, 2019, **9**, 36771–36787.
35 *Raman Spectroscopy for Nanomaterials Characterization*, ed. C. S. S. R. Kumar, Springer Berlin Heidelberg, Berlin, Heidelberg, 2012.
36 W. Liang, L. Chen, L. Wang, Y. Yin, Z. Li and H. Li, High pressure synthesis of siderite (FeCO3) and its thermal expansion coefficient, *High Temp. - High Pressures*, 2018, **47**, 153–164.
37 P. Tan, Y. Deng and Q. Zhao, Temperature-dependent Raman spectra and anomalous Raman phenomenon of highly oriented pyrolytic graphite, *Phys. Rev. B: Condens. Matter Mater. Phys.*, 1998, **58**, 5435–5439.
38 V. A. Sethuraman, L. J. Hardwick, V. Srinivasan and R. Kostecki, Surface structural disordering in graphite upon lithium intercalation/deintercalation, *J. Power Sources*, 2010, **195**, 3655–3660.
39 J. Stöhr, *NEXAFS Spectroscopy*, Springer Berlin, Heidelberg, 1992, vol. 25.
40 E. Voloshina, R. Ovcharenko, A. Shulakov and Y. Dedkov, Theoretical description of X-ray absorption spectroscopy of the graphene-metal interfaces, *J. Chem. Phys.*, 2013, **138**, 154706.
41 C. Ehlert, W. E. S. Unger and P. Saalfrank, C K-edge NEXAFS spectra of graphene with physical and chemical defects: a study based on density functional theory, *Phys. Chem. Chem. Phys.*, 2014, **16**, 14083–14095.
42 P. A. Brühwiler, *et al.*, π^* and σ^* Excitons in C 1 s Absorption of Graphite, *Phys. Rev. Lett.*, 1995, **74**, 614–617.
43 Y. Ahmad, *et al.*, NMR and NEXAFS Study of Various Graphite Fluorides, *J. Phys. Chem. C*, 2013, **117**, 13564–13572.
44 S. Sainio, *et al.*, Trends in Carbon, Oxygen, and Nitrogen Core in the X-ray Absorption Spectroscopy of Carbon Nanomaterials: A Guide for the Perplexed, *J. Phys. Chem. C*, 2021, **125**, 973–988.
45 E. E. Groopman and L. R. Nittler, Correlated XANES, TEM, and NanoSIMS of presolar graphite grains, *Geochim. Cosmochim. Acta*, 2018, **221**, 219–236.

46 E. Groopman, L. R. Nittler, T. Bernatowicz and E. Zinner, Nanosims, tem, and xanes studies of a unique presolar supernova graphite grain, *ApJ*, 2014, **790**, 9.
47 S. Bernard, *et al.*, XANES, Raman and XRD study of anthracene-based cokes and saccharose-based chars submitted to high-temperature pyrolysis, *Carbon*, 2010, **48**, 2506–2516.
48 Z. Shpilman, *et al.*, A near edge X-ray absorption fine structure study of oxidized single crystal and polycrystalline diamond surfaces, *Diamond Relat. Mater.*, 2014, **45**, 20–27.
49 R. V. Dennis, *et al.*, Near-edge x-ray absorption fine structure spectroscopy study of nitrogen incorporation in chemically reduced graphene oxide, *J. Vac. Sci. Technol., B: Nanotechnol. Microelectron.:Mater., Process., Meas., Phenom.*, 2013, **31**, 041204.
50 D. A. Outka, J. Stöhr, R. J. Madix, H. H. Rotermund, B. Hermsmeier and J. Solomon, NEXAFS studies of complex alcohols and carboxylic acids on the Si (111)(7 × 7) surface, *Surf. Sci.*, 1987, **185**(1–2), 53–74.
51 J. Díaz, S. Anders, A. Cossy-Favre, M. Samant and J. Stöhr, Enhanced secondary electron yield from oxidized regions on amorphous carbon films studied by x-ray spectromicroscopy, *J. Vac. Sci. Technol., A*, 1999, **17**, 2737–2740.
52 S. Sainio, *et al.*, What Does Nitric Acid Really Do to Carbon Nanofibers?, *J. Phys. Chem. C*, 2016, **120**, 22655–22662.
53 S. Sainio, *et al.*, Correlation between sp^3 -to-sp^2 Ratio and Surface Oxygen Functionalities in Tetrahedral Amorphous Carbon (ta-C) Thin Film Electrodes and Implications of Their Electrochemical Properties, *J. Phys. Chem. C*, 2016, **120**, 8298–8304.
54 M. K. Rabchinskii, *et al.*, Guiding graphene derivatization for covalent immobilization of aptamers, *Carbon*, 2022, **196**, 264–279.
55 S. J. Rezvani, *et al.*, Structural anisotropy in three dimensional macroporous graphene: A polarized XANES investigation, *Diamond Relat. Mater.*, 2021, **111**, 108171.
56 R. P. Gandhiraman, *et al.*, X-ray Absorption Study of Graphene Oxide and Transition Metal Oxide Nanocomposites, *J. Phys. Chem. C*, 2014, **118**, 18706–18712.
57 K. H. Stone, *et al.*, Remote and automated high-throughput powder diffraction measurements enabled by a robotic sample changer at SSRL beamline 2-1, *J. Appl. Crystallogr.*, 2023, **56**, 1480–1484.
58 A. A. Coelho, *TOPAS* and *TOPAS-Academic*: an optimization program integrating computer algebra and crystallographic objects written in C, *J. Appl. Crystallogr.*, 2018, **51**, 210–218.
59 B. Ravel and M. Newville, ATHENA, ARTEMIS, HEPHAESTUS: data analysis for X-ray absorption spectroscopy using IFEFFIT, *J. Synchrotron. Rad.*, 2005, **12**, 537–541.
60 G. Landrot and E. Fonda, *Fastosh*: a software for the treatment of XAFS datasets of environmental relevance or acquired in *operando* conditions, *J. Synchrotron. Rad.*, 2025, **32**, 1085–1094.